Processing and Application of Ceramics 11 [4] (2017) 304–310
https://doi.org/10.2298/PAC1704304M



# Influence of Mg doping on structural, optical and photocatalytic performances of ceria nanopowders

Branko Matović[1,*], Jelena Luković[1], Bojan Stojadinović[2], Sonja Aškrabić[2], Aleksandra Zarubica[3], Biljana Babić[1], Zorana Dohčević-Mitrović[2]

[1]*Institute for Nuclear Sciences, Centre of Excellence-CextremeLab Vinca, University of Belgrade, Belgrade, Serbia*
[2]*Institute of Physics Belgrade, Pregrevica 118, University of Belgrade, Belgrade, Serbia*
[3]*Faculty of Sciences and Mathematics, Department of Chemistry, University of Nis, Nis, Serbia*

Received 21 July 2017; Received in revised form 14 November 2017; Accepted 6 December 2017

## Abstract

*Nanosized Mg-doped ceria powders were obtained by self-propagating room temperature reaction without using surfactants or templates. X-ray diffraction analysis and field emission scanning microscopy results showed that the doped samples are solid solutions with fluorite-type structure and spherical morphology. Raman spectra revealed an increase in the amount of oxygen vacancies with the increase of Mg concentration. This increasing results in a narrowing of the bandgap of $CeO_2$. The photocatalytic performances of the Mg-doped ceria solid solutions were evaluated by decomposing an organic dye, crystal violet under UV irradiation. The Mg-doped ceria solid solutions exhibit significantly better photocatalytic activity than the pure $CeO_2$ and commercial $TiO_2$. The higher first rate constant of the Mg-doped samples demonstrated that they are much more efficient than $TiO_2$ and $CeO_2$ under UV light. $Mg^{2+}$ dopant ions and oxygen vacancies play a significant role in the enhancement of photocatalytic performances of the Mg-doped ceria.*

***Keywords:*** *ceria, solid solution, oxygen vacancies, UV light illumination, nanocatalysis*

## I. Introduction

Nano ceria ($CeO_2$) has been extensively studied as an active or supporting catalytic material due to its superior oxygen storage-and-release properties [1]. Since ceria is a good electron acceptor, it can provide lattice oxygen in chemical reactions because of lower formation energy for oxygen vacancy [2–4]. Also, $CeO_2$ promotes the chemical activity of the material by facilitating electron transfer from suitable adspecies into an oxide surface [5,6]. A higher catalytic activity is related to the type, size, and distribution of oxygen vacancies. It is demonstrated that surface defects were more readily formed in $CeO_2$ nanostructures with special morphology, such as cubes, nanobelts, nanowires and nanotubes. Therefore, for the design of ceria based materials with high oxygen storage and transport capacity, it is important to know how to increase the number of structural defects (oxygen vacancies) and to maintain at the same time a fluorite-type crystal structure. This can be done either by the promotion of $Ce^{4+}$ reduction into $Ce^{3+}$ or by doping with transition or rare-earth elements [7]. $CeO_2$ is not generally considered as a photocatalytic material due to its wide band gap and specific 4f electron configuration. Despite the fact that little work was carried out in the field of photocatalytic applications of $CeO_2$ [8–10] recent studies demonstrated that improvement of ceria photocatalytic properties can be done by proper choice of dopant elements and their incorporated amounts [11] or by creating surface defects as the most reacting sites which can enhance the visible light activity of nanostructured ceria [12]. In addition, the preparation methods have also a significant influence on the ceria structure (homogeneity, morphology, grain size, crystal defects etc.) and its optical and photocatalytic properties. Therefore, tuning the band gap energy and tailoring the reactivity of ceria-based catalysts is still a challenging task.

*Corresponding authors: tel/fax: +381 11 3408 224
e-mail: *mato@vinca.rs*

In this work the Mg-doped ceria nonpowdered solid solutions ($Ce_{1-x}Mg_xO_{2-\delta}$, $0 \le x \le 0.4$) were prepared by facile and cost-effective self-propagating room temperature reaction (SPRT). The influence of Mg content on structural, optical and photocatalytic properties was examined. The evaluation of photocatalytic activity of synthesized catalysts has been carried out by degradation of crystal violet as a model pollutant. The mechanism for the band gap narrowing of Mg-doped ceria and the enhancement of the photocatalytic performances are also proposed.

## II. Materials and methods

The solid solutions of magnesium-doped samples were prepared by a SPRT method using metal nitrates and sodium hydroxide as the starting materials. This technique gives the possibility of producing very fine powders with very precise stoichiometry in accordance with the tailored compositions [13–16]. Preparation of $Ce_{1-x}Mg_xO_{2-\delta}$ powders was performed by hand mixing chemicals according to:

$$2\,[(1-x)Ce(NO_3)_3 \cdot 6\,H_2O + xMg(NO_3)_2 \cdot 6\,H_2O] + 6\,NaOH + \\ + (\tfrac{1}{2}-\delta)O_2 \longrightarrow 2\,Ce_{1-x}Mg_xO_{2-\delta} + 6\,NaNO_3 + 15\,H_2O \quad (1)$$

The compositions of the reacting mixtures were calculated according to the nominal composition of the final reaction product. Compositions of $Ce_{1-x}Mg_xO_{2-\delta}$ were synthesized with $x$ ranging from 0.0 to 0.4. The described reaction belongs to a group of double exchange reactions and develops spontaneously after being initiated, terminating extremely rapidly. After the mixture of reactants ($Ce(NO_3)_3 \cdot 6\,H_2O$, Aldrich, $Mg(NO_3)_2 \cdot 6\,H_2O$, Aldrich) was mechanically activated (by hand mixing instead by heating) the reaction took place at room temperature and terminated very quickly. The obtained mixtures of reaction products according to Eq. (1) were subjected to a centrifuge treatment to eliminate $NaNO_3$ and drying at 80 °C.

After drying, the composition of the solid solutions was identified by means of powder XRD on a Rigaku IV, XRD diffractometer with CuK$\alpha$ radiation at room temperature. The average crystallite size was measured from the 111 XRD peak using the Scherrer formula. The values of the unit cell parameters of all the analysed powders are calculated on the basis of the equation:

$$\frac{4\sin^2\theta}{\lambda^2} = \frac{1}{d_{hkl}^2} = \frac{h^2+k^2+l^2}{a^2} \quad (2)$$

where $\theta$ is the Bragov angle, $hkl$ are Miller indices, $\lambda$ is the wavelength (1.54184 Å), and $a$ is parameter of the unit cell of the crystal [17].

SEM analysis using Zeiss DSM 982 Gemini scanning electron microscope proved that the obtained powders were in the nanometric size range. The room-temperature Raman spectra were obtained using a U-1000 (Jobin-Ivon) double monochromator in back scattering geometry. The Raman spectra were excited by the 514 nm line of an $Ar^+/Kr^+$ ion laser operating at low incident power (~20 mW) in order to avoid sample heating. The measurements of UV-Vis absorption spectra of the samples were carried out on a Specord M40 Carl Zeiss spectrophotometer in a spectral range 200–600 nm, at room temperature.

The specific surface area and the pore size distribution (PSD) of the doped $CeO_2$ samples were analysed using the Surfer (Thermo Fisher Scientific, USA). PSD was estimated by applying BJH method [18] to the desorption branch of isotherms and mesopore surface and micropore volume were estimated using the $t$-plot method [19].

Photocatalytic activity of the synthesized Mg-doped samples was evaluated by the degradation of crystal violet (CV) under UV light irradiation. The photochemical reactor consisted of UV lamp (Roth Co., 16 W, 2.5 mW/cm$^2$, $\lambda_{max}$ = 366 nm) positioned annularly to the 50 ml quartz flask. The acidity of solutions was not additionally adjusted and pH values were in the range from 6.7 to 7.0. The rates of photocatalytic degradations of CV were followed at initial concentration of 0.01 mmol/dm$^3$. The amount of used catalyst was 30 ± 2 mg. CV photolysis test was performed prior to photocatalytic measurements and no significant dye degradation was observed. The prepared $Ce_{1-x}Mg_xO_{2-\delta}$ samples were immersed into CV solution and the solution was continuously stirred and kept in the dark for 1 h to establish adsorption-desorption equilibrium before being irradiated. Photocatalytic activity of the $Ce_{1-x}Mg_xO_{2-\delta}$ solid solutions were compared to commercial standard $TiO_2$ sample - Degussa P25 (having specific surface area, $S_{BET}$, of 56 m$^2$/g, pore volume of 0.25 cm$^3$/g, average pore size of 17.5 nm, crystallite size of 21 nm and the following phase composition: anatase, 81 vol.% and rutile, 19 vol.%) and the undoped $CeO_2$ sample.

The reaction rate constant ($k$) was determined assuming quasi first order kinetics using the following equation:

$$\ln\frac{C_0}{C_t} = k \cdot t \quad (3)$$

where $C_0$ is the initial dye concentration, $C_t$ is the concentration at time $t$. The slope of the $\ln(C_0/C_t)$ versus time plot gives the value for the rate constant $k$.

## III. Results

### 3.1. Characterization of Mg-doped ceria

XRD spectra of the $Ce_{1-x}Mg_xO_{2-\delta}$ samples, presented in Fig. 1, revealed that the obtained powders are a single phase with the fluorite crystal structure. Main diffraction peaks in each sample were significantly broadened indicating small crystallite size and/or strain. New peak is observed for the sample doped with 40 at.% of Mg, indicating that the limit of Mg solubility in ceria crystal lattice is in the range from 30 to 40 at.%. This high sol-

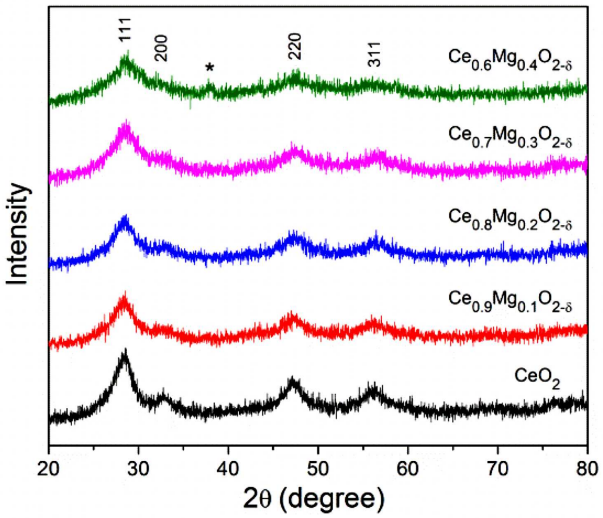


**Figure 1. X-ray diffraction patterns of synthesized of $Ce_{1-x}Mg_xO_{2-\delta}$ nanopowders (* - brucite phase)**

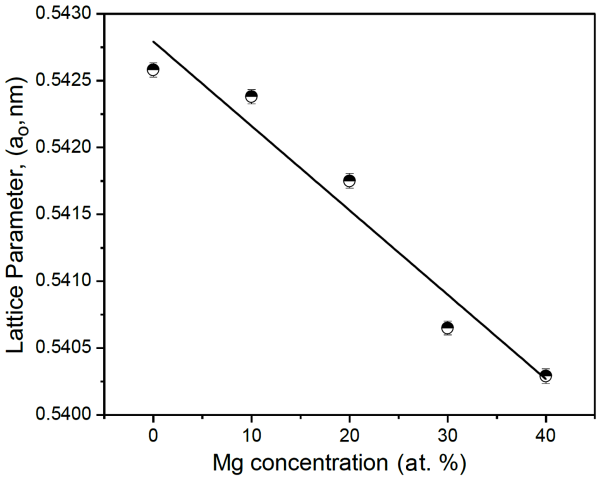


**Figure 2. Lattice parameter ($a_0$) $Ce_{1-x}Mg_xO_{2-\delta}$ samples as a function of Mg content**

ubility may be attributed to the nanometric nature of the obtained powders. Excess of Mg is very reactive and in contact with moisture make a brucite phase $Mg(OH)_2$, marked with asterisks in Fig. 1. XRD spectra exhibit very diffuse diffraction lines with increasing Mg content, which makes difficult to indicate precisely some atomic planes (*hkl*: 200, 220, 311, 420).

Calculation of cell parameters (Fig. 2) based on X-ray results, shows the linear dependence of unit cell parameter versus concentration of $Mg^{2+}$ ions. With increasing of $Mg^{2+}$ ion concentration the cubic ceria lattice shrinks. According to Shannon's compilation [19], the ionic radii of $Ce^{4+}$ and $Mg^{2+}$ for coordination number (CN) 8, are 0.97 and 0.89 Å, respectively. Thus, doping with a smaller sized $Mg^{2+}$ ion and increasing of dopant concentration, will lead to the contraction of the ceria lattice. Also, lattice parameter ($a_0$) of doped ceria versus $Mg^{2+}$ content, obeys Vegard's law, implying that $Mg^{2+}$ substitutionally entered into ceria lattice. The crystallite size, calculated on the basis of XRD data, for all powders is less than 5 nm.

Room-temperature Raman spectra of the Mg-doped ceria are presented in Fig. 3, whereas in the inset is given the Raman spectrum of the undoped $CeO_2$. Room-temperature Raman spectrum of the undoped $CeO_2$ sample shows the strong peak at ~455 $cm^{-1}$ corresponding to the triply degenerate $F_{2g}$ mode characteristic for the fluorite cubic $CeO_2$ structure. The red shift of this mode compared to its bulk counterpart (464 $cm^{-1}$) and pronounced asymmetry on the low-energy side originates from the phonon confinement, strain and the presence of defects [20,21]. In the sample doped with 10 at.% of Mg, $F_{2g}$ mode is shifted to ~457 $cm^{-1}$, due to the substitutional incorporation of Mg, as ion of smaller ionic radius, into ceria lattice. With further increasing of Mg content, $F_{2g}$ mode shifts to higher energies and in the 40 at.% Mg doped sample, this mode is positioned at ~460 $cm^{-1}$.

Another mode of lower intensity, positioned at ~600 $cm^{-1}$, is characteristic for nanometric ceria and is attributed to the presence of intrinsic oxygen vacancies [20,22], due to the partial reduction of $Ce^{4+}$ to $Ce^{3+}$. This mode is also presented in the Mg-doped samples. From the Lorentzian fit procedure (insets in Fig. 3), it

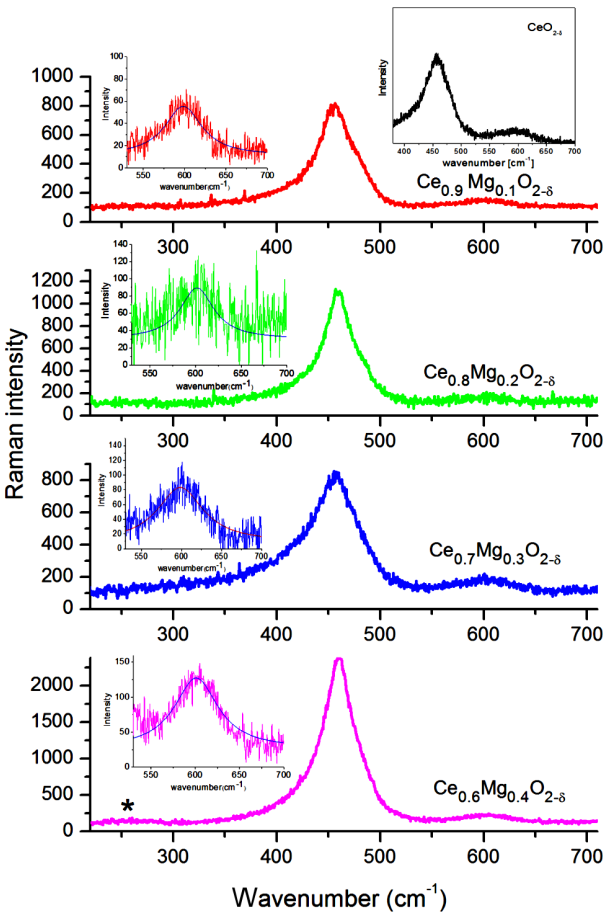


**Figure 3. Room temperature Raman spectra of Mg-doped samples (insets present Raman spectrum of undoped $CeO_2$ and Lorentzian fits of intrinsic vacancy mode)**

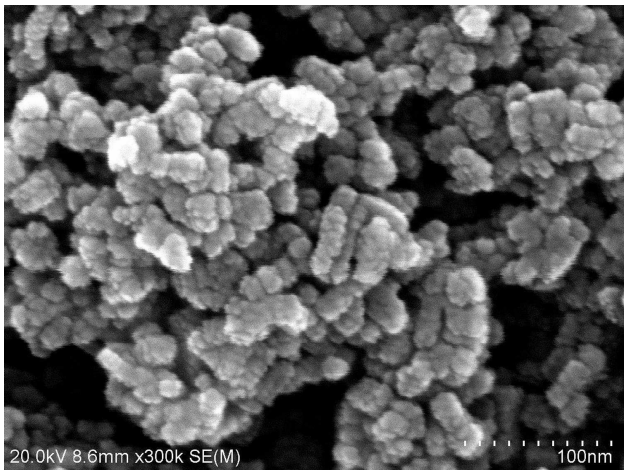


**Figure 4. Typical FESEM images of 20 at.% Mg-doped ceria sample**

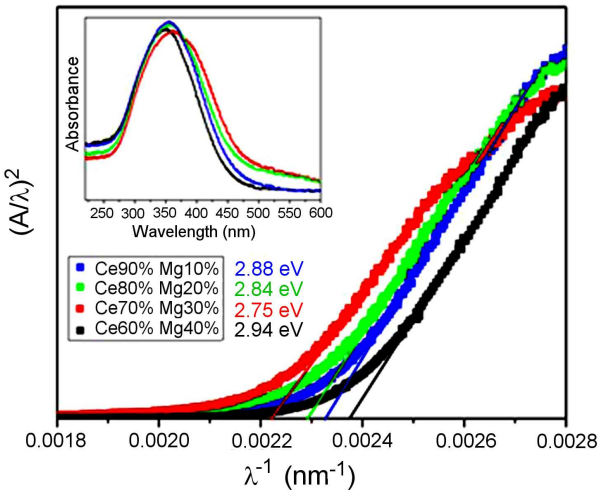


**Figure 5. $(A/\lambda)^2$ plots for Mg-doped samples (inset presents absorption spectra of doped samples)**

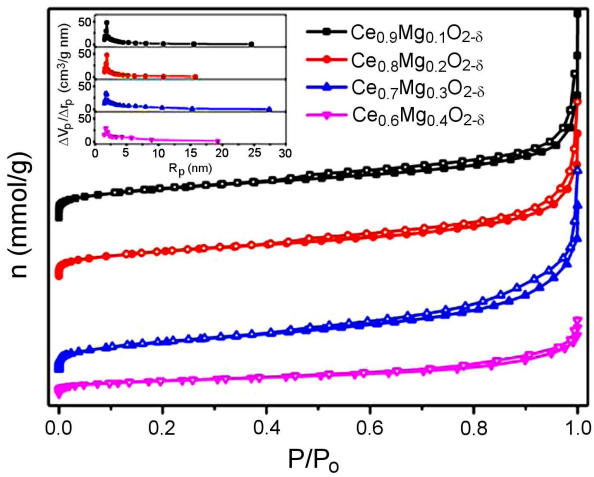


**Figure 6. $N_2$ adsorption (solid symbols)/desorption (open symbols) isotherms and the pore size distribution (inset) of Mg-doped samples**

was obtained that intensity of this mode increases with an increase of Mg content, pointing at increased intrinsic oxygen vacancy concentration [22]. In the spectra of the sample with 40 at.% Mg, new broad, low intensity mode around 270 $cm^{-1}$ is observed. This mode (marked with asterisks in Fig. 3) can be ascribed to the $E_g$ mode of $Mg(OH)_2$ (brucite) phase, which is in good agreement with XRD measurement [23]. It is evident from the Raman spectra of the sample with 40 at.% Mg that limits of Mg solubility in ceria crystal lattice is less than 40 at.%.

The as-prepared ceria powders consist of rounded particles with size less than 10 nm, roughly estimated (Fig. 4). The particles are linked in the form of blackberry, which together form cauliflower morphology. There is no difference of morphology and particle size between the Mg-doped ceria samples. It seems that various doping concentration has no influence on the microstructure of the powders.

The optical band gap of the undoped $CeO_2$, which corresponds to the O 2p ⟶ Ce $4f^0$ transition, was previously determined to be around 3.6 eV [24]. From the absorption spectra of the solid solutions $Ce_{1-x}Mg_xO_{2-\delta}$ ($x$ = 0.1, 0.2, 0.3 and 0.4), presented in the inset of Fig. 5, the band gap energies of the Mg-doped samples were obtained using Tauc law for direct transition and applying absorption spectrum fitting method [25]. The plots of $(A/\lambda)^2$ vs. $1/\lambda$ are presented in Fig. 5, where $A$ is the absorbance and $\lambda$ is the wavelength. The linear extrapolation of $(A/\lambda)^2$ to zero gives a wavelength $\lambda_g$ which corresponds to the optical band gap. The band gap values can be obtained using well known relation $E_g = 1240/\lambda_g$. The estimated direct band gap values ($E_g$) for $Ce_{1-x}Mg_xO_{2-\delta}$ samples are given in Fig. 5. It can be seen that with Mg doping up to 30 at.% band gap values decreased from 2.88 to 2.75 eV due to the formation of defect (localized) levels inside the gap with Mg doping [26]. In the sample with 40 at.% of Mg dopant the $E_g$ is slightly increased to 2.94 eV. Such an increase can be a consequence of the presence of $Mg(OH)_2$ phase which has higher band gap value than $CeO_2$ [27] or to the Burstein-Moss effect caused by increased electron concentration and lifting of the Fermi-level because of increased Mg content and oxygen vacancies concentration [28].

Nitrogen adsorption/desorption isotherms for the Mg-doped samples, are shown in Fig. 6. According to the IUPAC classification [29] isotherms of samples are of type IV and with a hysteresis loop which is associated with mesoporous materials. In all samples, the shape of hysteresis loop is of type H3. Isotherms revealing type H3 hysteresis do not exhibit any limiting adsorption at high $P/P_0$, which is observed with non-rigid aggregates of plate-like particles giving rise to slit-shaped pores [30]. Specific surface areas calculated by BET equation, $S_{BET}$, are listed in Table 1. $S_{BET}$ values for all Mg-doped samples are comparable (between 110–120 $m^2/g$), i.e. the amount of dopant does not have

**Table 1. Porous properties of $Ce_{1-x}Mg_xO_{2-\delta}$ nanopowders**

| Sample | $S_{BET}$ [$m^2/g$] | $S_{meso}$ [$m^2/g$] | $S_{mic}$ [$m^2/g$] | $V_{mic}$ [$cm^3/g$] | $r_m$ [nm] |
|---|---|---|---|---|---|
| $CeO_2$ | 70 | 45 | 25 | 0.013 | - |
| $Ce_{0.9}Mg_{0.1}O_2$ | 114 | 104 | 10 | 0.003 | 3.7 |
| $Ce_{0.8}Mg_{0.2}O_2$ | 110 | 110 | 0 | 0 | 4.3 |
| $Ce_{0.7}Mg_{0.3}O_2$ | 120 | 120 | 0 | 0 | 5.2 |
| $Ce_{0.6}Mg_{0.4}O_2$ | 113 | 113 | 0 | 0 | 4.4 |

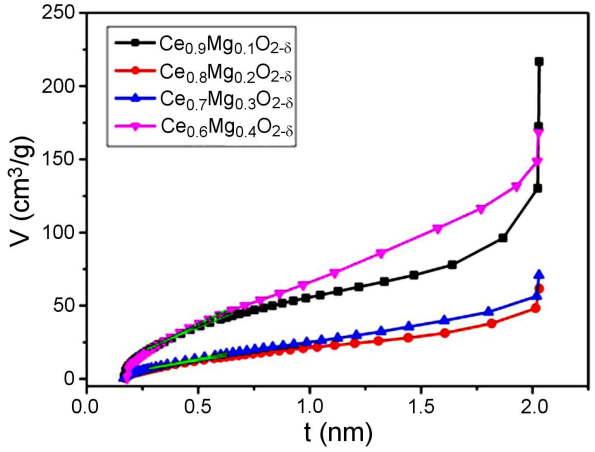


**Figure 7. *t*-plots of Mg-doped samples**

an essential influence on the overall specific surface area of the doped nanopowders. On the contrary, the undoped ceria sample has significantly smaller specific surface area than the doped ones. Therefore, the Mg doping increases the porosity of ceria. Pore size distribution (PSD) of samples possesses sharp PSD peak with most of the pore radius between 2–20 nm (inset of Fig. 6) implying that the samples are mesoporous. Values of mean pore radius, for all samples, are presented in Table 1.

The *t*-plot, obtained on the basis of the standard nitrogen adsorption isotherm, is shown in Fig. 7. The straight line in the medium *t*-plot region gives a mesoporous surface area including the contribution of the external surface, $S_{meso}$, determined by its slope, and the micropore volume, $V_{mic}$, which is given by the intercept. The calculated porosity parameters ($S_{meso}$, $S_{mic}$, $V_{mic}$) are given in Table 1. *t*-plot analysis confirmed that all samples are mesoporous, although a small amount of micropores (pore radius below 2 nm) was detected in the sample with 10 at.% of Mg and undoped ceria.

### *3.2. Photocatalytic performance of Mg-doped ceria*

The influence of the dopant concentration on the photocatalytic activity of the Mg-doped ceria nanopowders has been studied through the photocatalytic removal of organic dye crystal violet (CV) under UV light irradiation. The kinetics of degradation of CV is represented in Fig. 8. As can be seen from Fig. 8, the pure ceria has shown modest photocatalytic activity. With increasing Mg content, the degradation of CV became significant. The samples with higher Mg content (>10 at.% Mg) have shown even better photocatalytic activity than

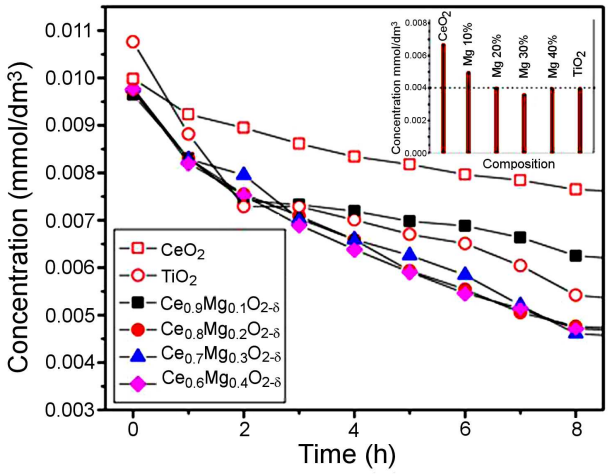


**Figure 8. Photocatalytic degradation of CV in the presence of $Ce_{1-x}Mg_xO_{2-\delta}$ nanopowders and $TiO_2$ (insert represents photocatalytic efficiency after 24 h)**

the commercial $TiO_2$ Degussa P25, which is known as one of the most efficient photocatalysts for dye degradation.

The reaction kinetics from Fig. 8, follows the first order and the degradation rate constants for 30 and 40 at.% Mg-doped samples, together with $TiO_2$ and $CeO_2$ as reference samples, are summarized in Table 2. It can be seen that the degradation rate constant for the $Ce_{0.7}Mg_{0.3}O_{2-\delta}$ and $Ce_{0.6}Mg_{0.4}O_{2-\delta}$ samples are higher than reference samples, implying that higher concentration of Mg in $CeO_2$ lattice improves the photocatalytic efficiency of ceria.

**Table 2. The pseudo-first rate constants for CV after exposition time of 8 h**

| Sample | $k$ [$h^{-1}$] | $R^2$ |
|---|---|---|
| $Ce_{0.7}Mg_{0.3}O_{2-\delta}$ | 0.081 | 0.980 |
| $Ce_{0.6}Mg_{0.4}O_{2-\delta}$ | 0.078 | 0.998 |
| $CeO_2$ | 0.026 | 0.982 |
| $TiO_2$ | 0.056 | 0.910 |

After 24 h the photocatalytic activity of the solid solutions with concentrations of 20 and 40 at.% of Mg respectively, are the same as a $TiO_2$ standard, whereas the $Ce_{0.7}Mg_{0.3}O_{2-\delta}$ sample exhibited higher activity (inset of Fig. 8). Such high photocatalytic activity of the $Ce_{0.7}Mg_{0.3}O_{2-\delta}$ sample can be attributed to its large specific surface area, the largest one among all the studied nanopowders, regular mesoporosity and favourable average pore size. A slightly lower photocatalytic activity of the ceria sample with 40 at.% Mg can be explained by the appearance of secondary brucite phase.

In Fig. 9 an illustration of the proposed mechanism of photocatalytic reactions is given. Upon UV light illumination photogenerated electrons and holes can be trapped by dopant ions, i.e. $Mg^{2+}$ ions can be electron acceptors and/or hole donors. Reduction of the band gap of the Mg-doped samples implies that $Mg^{2+}$ ions introduce states into the band gap of $CeO_2$. In such a

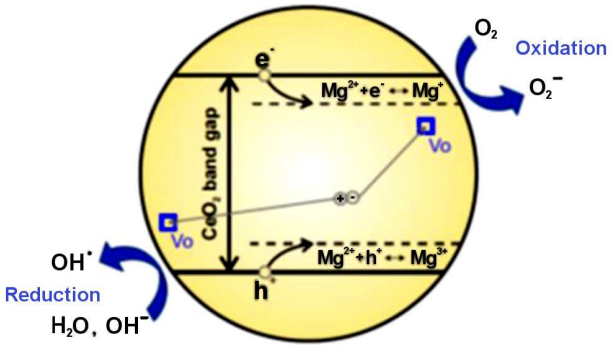


**Figure 9. Illustration of the photocatalytic mechanism at Mg-doped $CeO_2$ interface under the UV light irradiation**

way, Mg doping could be effective in delay of electron-hole recombination process, increasing the lifetime of the charge separation. The trapped electrons can be subsequently scavenged by molecular oxygen, which is adsorbed on the $CeO_2$ surface, to generate the superoxide radical ($O_2^{-\bullet}$). Superoxide radicals in contact with $H_2O$ molecules form $OH^-$ ions and finally $OH^\bullet$ radicals, which attack the dye in aqueous solution leading to its degradation. Due to high oxidative potential, the positive holes act as good oxidizing agents for dye degradation. The trapped holes can directly attack the dye or can interact with $OH^-$ or water molecules present on the surface of the catalyst forming hydroxyl radicals ($OH^\bullet$).

Ceria nanoparticles are prone to the formation of oxygen vacancies (VO) which promote the formation of $Ce^{3+}$ ions in the grain boundary region [30]. In order to attain charge neutrality with Mg doping, oxygen vacancies will be created in the ceria lattice. This fact is confirmed from Raman measurements. $V_O$ as defects can also introduce localized state below the conduction band of $CeO_2$ [24] reducing the band gap. Furthermore, a high concentration of surface donor defects ($V_O$ and $Ce^{3+}$) can serve as charge carrier traps and adsorption sites which transfer charge to adsorbed species like $O_2$ or $H_2O$ on ceria surface. In such a way, oxygen vacancies can delay the electron-hole recombination process and support the charge carrier transfer to the ceria surface, improving the photocatalytic efficiency of ceria. Theoretical and experimental results on $TiO_2$ and ZnO have shown that excess electrons localized on the oxygen vacancy states affect surface adsorption and increase photocatalytic activity of $TiO_2$ and ZnO [31,32]. Therefore, it is reasonable to assume that besides $Mg^{2+}$ ions as trapping centres, oxygen vacancies have a strong impact on the increased photocatalytic activity of Mg-doped ceria.

## IV. Conclusions

Mg-doped ceria nanopowders ($Ce_{1-x}Mg_xO_{2-\delta}$, $0 \leq x \leq 0.4$) have been successfully fabricated via self-propagating room temperature reaction without any surfactant or template. The obtained samples are of fluorite cubic structure, composed of rounded particles with size less than 10 nm with the higher specific surface area than the pure $CeO_2$. Substitutional doping with lower valence $Mg^{2+}$ ions promotes the formation of oxygen vacancies in ceria lattice, the amount of which increases with an increase of dopant concentration. The increased dopant concentration results in an effective red shift of the band gap value of the $Ce_{1-x}Mg_xO_{2-\delta}$ samples due to the formation of localized states inside the ceria gap. Only the sample with 40 at.% of Mg exhibited slight blueshift of the band gap due to the appearance of brucite phase. The photocatalytic activity of the Mg-doped $CeO_2$ for degradation of azodye crystal violet was examined under UV light irradiation. It was found that the samples with Mg content higher than 10 at.% have much better photocatalytic performances than the undoped $CeO_2$ and commercial Degussa P25. Localized electronic states of $Mg^{2+}$ ions and oxygen vacancies can capture photogenerated charge carriers delaying recombination process, but can also serve as active sites on ceria surface to transfer charge to adsorbed species like $O_2$ or $H_2O$ forming reactive radicals.

**Acknowledgement:** This work was financially supported by the Ministry of Education, Science and Technological Development of the Republic of Serbia under the projects III 45012 and ON171032. The authors would like to thank Nenad Tadić, Faculty of Physics, University of Belgrade for the UV-Vis measurements.

## References

1. G.A. Deluga, J.R. Salge, L.D. Schmidt, X.E. Verykios, "Renewable hydrogen from ethanol by autothermal reforming", *Science*, **303** (2004) 993–997.
2. M.V. Ganduglia-Pirovano, J.L.F.D. Silva, J. Sauer, "Density-functional calculations of the structure of near-surface oxygen vacancies and electron localization on $CeO_2$ (111)", *Phys. Rev. Lett.*, **102** (2009) 026101.
3. A. Migani, G.N. Vayssilov, S.T. Bromley, F. Illas, K.M. Neyman, "Greatly facilitated oxygen vacancy formation in ceria nanocrystallites", *Chem. Commun.*, **46** (2010) 5936–5938.
4. M. Nolan, S.C. Parker, G.W. Watson, "The electronic structure of oxygen vacancy defects at the low index surfaces of ceria", *Surface Sci.*, **595** (2005) 223–232.
5. G.N. Vayssilov, Y. Lykhach, A. Migani, T. Staudt, G.P. Petrova, N. Tsud, T. Skala, A. Bruix, F. Illas, K.C. Prince, V. Matolin, K.M. Neyman, J. Libuda, "Support nanostructure boosts oxygen transfer to catalytically active platinum nanoparticles", *Nature Mater.*, **10** (2011) 310–315.
6. M. Baron, H. Abbott, O. Bondarchuk, D. Stacchiola, A. Uhl, S. Shaikhutdinov, H.J. Freund, C. Popa, M.V.G. Pirovano, A.J. Sauer, "Resolving the atomic structure of vanadia monolayer catalysts: Monomers, trimers, and oligomers on ceria", *Angewandte Chemie Int. Edition*, **48** (2009) 8006–8009.
7. M. Mogenson, N.M. Sammes, G.A. Tompsett, "Physical, chemical and electrochemical properties of pure and doped ceria ", *Solid State Ionics*, **129** (2000) 63–94.
8. J.M. Coronado, A.J. Maira, A. Martínez-Arias, J.C. Conesa, J. Soria, "EPR study of the radicals formed upon

UV irradiation of ceria-based photocatalysts", *J. Photochem. Photobio. A: Chem.*, **150** (2002) 213–221.
9. G.R. Bamwenda, T. Uesigi, Y. Abe, K. Sayama, H. Arakawa, "The photocatalytic oxidation of water to $O^{-2}$ over pure $CeO_2$, $WO_3$, and $TiO_2$ using $Fe^{3+}$ and $Ce^{4+}$ as electron acceptors", *Appl. Catal. A: Gen.*, **205** (2001) 117–128.
10. M.D. Hernández-Alonso, A.B. Hungría, A. Martínez-Arias, M. Fernández-García, J.M. Coronado, J.C. Conesa, J. Soria, "EPR study of the photoassisted formation of radicals on $CeO_2$ nanoparticles employed for toluene photooxidation", *Appl. Catal. B: Environ.*, **50** (2004) 167–175.
11. L. Yue, X.-M. Zhang, "Structural characterization and photocatalytic behaviors of doped $CeO_2$ nanoparticles", *J. Alloys Compd.*, **475** (2009) 702–705.
12. M.M. Khan, S.A. Ansari, D. Pradhan, D.H. Han, J. Lee, M.H. Cho, "Defect-induced band gap narrowed $CeO_2$ nanostructures for visible light activities", *Ind. Eng. Chem. Res.*, **53** (2014) 9754–9763.
13. B. Matovic, Z. Dohcevic-Mitrovic, M. Radovic, Z. Brankovic, G. Brankovic, S. Boskovic, Z.V. Popovic, "Synthesis and characterization of ceria based nanometric powders", *J. Power Sources*, **193** (2009) 146–149.
14. B. Matovic, J. Pantic, J. Lukovic, S. Ilic, N. Stankovic, M. Kokunesovski, M. Miljevic, "Synthesis and characterization of (Ba,Yb) doped ceria nanopowders", *Process. Appl. Ceram.*, **5** (2011) 69–72.
15. M. Prekajski, Z. Dohčević-Mitrović, M. Radović, B. Babić, J. Pantić, A. Kremenović, B. Matović, "Nanocrystaline solid solution $CeO_2$-$Bi_2O_3$", *J. Eur. Ceram. Soc.*, **32** (2012) 1983–1987.
16. M. Stojmenović, S. Bošković, S. Zec, B. Babić, B. Matović, D. Bučevac, Z. Dohčević-Mitrović, F. Aldinger, "Characterization of nanometric multidoped ceria powders", *J. Alloys Compd.*, **507** (2010) 279–285.
17. Lj. Karanović, D. Poleti, *X-ray Structural Analysis*, Institute for Textbooks and Teaching Resources, Belgrade, 2003.
18. E.P. Barret, L.G. Joyner, P.P. Halenda, "The determination of pore volume and area distributions in porous substances. I. Computations from nitrogen isotherms", *J. Am. Chem. Soc.*, **73** (1951) 373–380.
19. B.C. Lippens, B.G. Linsen, J.H. d. Boer, "Studies on pore systems in catalysts I. The adsorption of nitrogen; apparatus and calculation", *J. Catal.*, **3** (1964) 32–37.
20. R.D. Shannon, "Revised effective ionic radii and systematic studies of interatomie distances in halides and chaleogenides", *Acta Crystallogra. Section A*, **32** [5] (1976) 751–767.
21. Z.D. Dohčević-Mitrović, M.J. Šćepanović, M.U. Grujić-Brojčin, Z.V. Popović, S.B. Bošković, B.M. Matović, M.V. Zinkevich, F. .Aldinger, "The size and strain effects on the Raman spectra of $Ce_{1-x}Nd_xO_{2-\delta}$ ($0 \le x \le 0.25$) nanopowders", *Solid State Commun.*, **137** (2006) 387–390.
22. P.J. Colomban, G. Gouadec, "Raman spectroscopy of nanostructures and nanosized materials", *J. Raman Spectrosc.*, **38** (2007) 598–603.
23. Z.D. Dohčević-Mitrović, M.U. Grujić-Brojčin, M.J. Šćepanović, Z.V. Popović, S.B. Bošković, B.M. Matović, M.V. Zinkevich, F. Aldinger, "$Ce_{1-x}Y(Nd)_xO_{2-\delta}$ nanopowders: potential materials for intermediate temperature SOFCs", *J. Phys.: Condens. Mat.*, **18** (2006) S2061–S2068.
24. P. Dawson, C.D. Hatfield, G.R. Wilkinson, "The polarized infra-red and Raman spectra of $Mg(OH)_2$ and $Ca(OH)_2$", *J. Phys. Chem. Solids*, **34** (1973) 1217–1225.
25. M. Radović, B. Stojadinović, N. Tomić, A. Golubović, B. Matović, I. Veljković, Z. Dohčević-Mitrović, "Investigation of surface defect states in $CeO_{2-y}$ nanocrystals by Scanning - tunneling microscopy /spectroscopy and ellipsometry", *J. Appl. Phys.*, **116** (2014) 234305.
26. N. Ghobadi, "Band gap determination using absorption spectrum fitting procedure", *Int. Nano Lett.*, **3** (2013) 1–4.
27. M. Radović, Z. Dohčević-Mitrović, A. Golubović, V. Fruth, S. Preda, M. Šćepanović, Z.V. Popović, "Influence of $Fe^{3+}$-doping on optical properties of $CeO_{2-y}$ nanopowders", *Ceram. Int.*, **39** (2013) 4929–4936.
28. K. Mageshwari, R. Sathyamoorthy, "Studies on photocatalytic performance of MgO nanoparticles prepared by wet chemical method", *Trans. Indian Instit. Metals*, **65** (2012) 49–55.
29. V. Etacheri, R. Roshan, V. Kumar, "Mg-doped ZnO nanoparticles for efficient sunlight-driven photocatalysis", *ACS Appl. Mater. Inter.*, **4** (2012) 2717–2725.
30. B. Choudhury, A. Choudhury, "$Ce^{3+}$ and oxygen vacancy mediated tuning of structural and optical properties of $CeO_2$ nanoparticles", *Mater. Chem. Phys.*, **131** (2012) 666–671.
31. F. Kayaci, S. Vempati, I. Donmez, N. Biyikliab, T. Uyar, "Role of zinc interstitials and oxygen vacancies of ZnO in photocatalysis: a bottom-up approach to control defect density", *Nanoscale*, **6** (2014) 10224–10234.
32. X. Pan, M.Q. Yang, X. Fu, N. Zhang, Y.J. Xu, "Defective $TiO_2$ with oxygen vacancies: synthesis, properties and photocatalytic applications", *Nanoscale*, **5** (2013) 3601–3614.